International Forum on Aeroelasticity and Structural Dynamics
IFASD 2019
9-13 June 2019, Savannah, Georgia, USA

APPROXIMATION OF AERODYNAMIC GEOMETRICAL NONLINEARITIES IN AIRCRAFT WITH HIGH-ASPECT-RATIO WINGS

Antônio B. Guimarães Neto[1]

[1]Instituto Tecnológico de Aeronáutica
São José dos Campos, SP, 12228-900, Brazil
antonio@ita.br

Keywords: aeroelasticity, flight dynamics, flexible aircraft, small deformations, aerodynamic geometrical nonlinearities

Abstract: An analysis of the flight dynamics of flexible aircraft having high-aspect-ratio wings shows that, even if the elastic deformations are not large enough to incur structural-dynamic geometrical nonlinearities, important aerodynamic effects can arise that are geometrically nonlinear in essence. For instance, the dihedral effect of the deformed wing is usually significantly different from that of the undeformed one, leading to unacceptable inaccuracies when analyzing the aircraft response to side gusts. Classical approaches to the aeroelastic modeling of flexible aircraft, using geometrically-linear finite elements, the vortex- or doublet-lattice methods, and linear or surface spline interpolation techniques, are unable to represent aerodynamic geometrical nonlinearities, because all the aeroelastic model matrices are calculated a priori for the undeformed aircraft and remain unchanged in the analysis. However, numerical experimentation indicates that, if small deformations occur, then the aerodynamic geometrical nonlinearities can be approximately modeled with an on-line update of the spline matrices to take into account the instantaneous deformed normal directions, without the need to perform the much costlier aerodynamic mesh deformation. This paper aims at the derivation of the equations for the modified generalized aerodynamic forces and at the validation of the proposed method in both static and dynamic conditions.

1 INTRODUCTION

Formulations for the flight dynamics of flexible aircraft based on the simplifying assumption of small deformations have long been available and frequently been used. Quasi-static analysis techniques as proposed by Rodden and Love [1] and implemented in MSC Nastran [2] are among the main uses of geometrically-linear aeroelastic finite-element method (FEM) models.

The simplifying assumption can also be considered in dynamically-coupled formulations, in which n elastic degrees of freedom (DOFs) are included to model the structural dynamics, and the number of flight-dynamic equations of motion (EOMs) increases from the classical six-degree-of-freedom (6-DOF), rigid-body system to a 6+n-DOF system. In this case, one of the greatest advantages of the assumption of small deformations is the possibility of using modal superposition with a small quantity of normal modes retained in the model [3–5], leading to significantly lower computational cost of numerical simulations than when compared with geometrically-nonlinear models.

Slightly-flexible aircraft flight-dynamic models based on small deformations have also been subjected to experimental validation. Silvestre and Luckner [6] e.g. demonstrated the applicability of a dynamically-coupled, linearized mean-axis formulation [5] for flight control law and aircraft design, based on favorable comparisons between simulation and flight-test data obtained with a prototype of the utility aircraft Stemme S15.

Recently, Guimarães Neto et al. [7, 8] assessed the range of validity of the assumption of small deformations in modeling the structural dynamics of flexible aircraft. Both a geometrically-linear (GL) and a geometrically-nonlinear (GN) formulation were used to obtain results for equilibrium conditions, linearized aircraft dynamics, and in nonlinear time-marching simulations. In the GN case, the aerodynamic mesh used in the vortex-lattice method (VLM) [9] was consistently updated with the aircraft deformation, with the aerodynamic normal forces then behaving as follower forces.

One of the main findings of the works was that, although the structural-dynamic model remains valid for deformations in bending that displace the wing tip by up to 12% of the wing semi-span, the aerodynamic model is more strongly influenced, leading to non-negligible differences in the results for smaller wing tip vertical displacements, on the order of 5% of the wing semi-span [7, 8].

However, updating the aerodynamic mesh in every instant of the simulation is a costly process, because it implies the need to recalculate the aerodynamic influence coefficient (AIC) matrix of the VLM, which might take more than one second of computing time for models with typically more than one thousand boxes (panels). The process becomes impracticable when it comes to models using unsteady aerodynamics, e.g., the doublet-lattice method (DLM) [10] and rational-function approximations (RFAs) [11], because, before the RFAs are calculated, the AIC matrices would need to be obtained for several different values of reduced frequency, a process that can take a few minutes of computing time.

Therefore, the alternative of keeping the AIC matrices and their RFAs constant seems very attractive for practical applications. Fortunately, numerical experimentation shows that, in the range of validity of small deformations in the structural-dynamic model, the AIC matrix of the VLM is almost constant. This can be understood because it is known that the major influence on a box is provided by the adjacent boxes [9], and the local geometry is not significantly affected by small deformations.

In this paper, an approximate methodology for modeling aerodynamic geometrical nonlinearities in aircraft with high-aspect-ratio wings is proposed. The methodology is based on updating not the aerodynamic mesh, but only the normal directions in which the normalwashes and aerodynamic forces are calculated for each box of the VLM or the DLM models. Additional terms caused by the noncoincidence of the deformed aerodynamic mesh and the undeformed structural-dynamic mesh are also taken into account.

The methodology implies the modification of the linear or surface spline matrices that are typically used in the interconnection between the aerodynamic and the structural-dynamic models. The use of spline interpolation is widespread in linear aeroelasticity mainly due to its relative simplicity and to its availability in commercial software like MSC Nastran [2].

The modified splines allow not only recalculating the generalized aerodynamic forces (GAFs) for the elastic DOFs considered in the analysis but, using the FEM model linear rigid-body modes, they also allow recalculating the rigid-body aerodynamic stability and control derivatives, which will then take into account the corrected normal directions for all the boxes of the VLM or DLM model.

In this paper, the six-meter-span configuration of the remotely-piloted X-HALE [12] aircraft will be analyzed. In Ref. [8], one of the findings was that this configuration is in the transition of small to large elastic deformations, with the latter frequently occurring in maneuvers. However, this aircraft almost always has significant aerodynamic geometrical nonlinearities present, leading to different responses when the aerodynamic mesh is updated or not.

The proposed technique will be demonstrated in several steps. The geometrically-nonlinear model will be used with and without updating the AIC matrix of the aerodynamic model, to show that the update is not necessary in a moderately-flexible aircraft. Then, equilibrium conditions will be calculated and flight simulations performed with the GN and the GL formulations, the latter both with and without the application of the proposed technique. To demonstrate the validity of the methodology, the stiffness of the aircraft structure is varied.

2 EQUATIONS OF MOTION

The geometrically-linear (GL) and the geometrically-nonlinear (GN) formulations used in this paper were described in Refs. [7, 8]. The GL formulation is based on Ref. [3]. There, the $6+n$ EOMs for the flexible aircraft were derived using Lagrange's equations, and they read:

$$
\begin{gathered}
m\dot{\mathbf{V}}_b + m\widetilde{\boldsymbol{\omega}_b}\mathbf{V}_b - m\widetilde{\mathbf{s}_{CG,b}}\dot{\boldsymbol{\omega}}_b - m\widetilde{\boldsymbol{\omega}_b}\widetilde{\mathbf{s}_{CG,b}}\boldsymbol{\omega}_b \\
+m\widetilde{\dot{\boldsymbol{\omega}}_b}\mathbf{D}_{CG,b}\mathbf{u}_G + 2m\widetilde{\boldsymbol{\omega}_b}\mathbf{D}_{CG,b}\dot{\mathbf{u}}_G \\
+m\widetilde{\boldsymbol{\omega}_b}\widetilde{\boldsymbol{\omega}_b}\mathbf{D}_{CG,b}\mathbf{u}_G + m\mathbf{D}_{CG,b}\ddot{\mathbf{u}}_G = m\mathbf{g}_b + \mathbf{F}_b + \Delta\mathbf{F}_b,
\end{gathered}
\tag{1}
$$

$$
\begin{gathered}
\mathbf{J}_{O,b}\dot{\boldsymbol{\omega}}_b + \widetilde{\boldsymbol{\omega}_b}\mathbf{J}_{O,b}\boldsymbol{\omega}_b + m\widetilde{\mathbf{s}_{CG,b}}\left(\dot{\mathbf{V}}_b + \widetilde{\boldsymbol{\omega}_b}\mathbf{V}_b\right) \\
+m\widetilde{\mathbf{D}_{CG,b}\mathbf{u}_G}\left(\dot{\mathbf{V}}_b + \widetilde{\boldsymbol{\omega}_b}\mathbf{V}_b\right) \\
+\Delta\mathbf{J}'_{O,b}\dot{\boldsymbol{\omega}}_b + \widetilde{\boldsymbol{\omega}_b}\Delta\mathbf{J}'_{O,b}\boldsymbol{\omega}_b + \Delta\dot{\mathbf{J}}'_{O,b}\boldsymbol{\omega}_b \\
+\dot{\mathbf{M}}_{\omega G}\dot{\mathbf{u}}_G + \mathbf{M}_{\omega G}\ddot{\mathbf{u}}_G + \widetilde{\boldsymbol{\omega}_b}\mathbf{M}_{\omega G}\dot{\mathbf{u}}_G \\
= m\widetilde{\mathbf{s}_{CG,b}}\mathbf{g}_b + m\widetilde{\mathbf{D}_{CG,b}\mathbf{u}_G}\mathbf{g}_b + \mathbf{M}_{O,b} + \Delta\mathbf{M}_{O,b},
\end{gathered}
\tag{2}
$$

$$
\begin{gathered}
\mathbf{M}_{GG}\ddot{\mathbf{u}}_G + \mathbf{B}_{GG}\dot{\mathbf{u}}_G + \mathbf{K}_{GG}\mathbf{u}_G \\
+m{\mathbf{D}_{CG,b}}^T\left(\dot{\mathbf{V}}_b + \widetilde{\boldsymbol{\omega}_b}\mathbf{V}_b\right) + {\mathbf{M}_{\omega G}}^T\dot{\boldsymbol{\omega}}_b \\
+2\dot{\mathbf{M}}^T_{\omega G}\boldsymbol{\omega}_b - \frac{1}{2}\sum_{g=1}^{n}\mathbf{e}_{n,g}{\boldsymbol{\omega}_b}^T\frac{\partial\Delta\mathbf{J}_{O,b}}{\partial u_g}\boldsymbol{\omega}_b \\
= m{\mathbf{D}_{CG,b}}^T\mathbf{g}_b + \mathbf{Q}_G.
\end{gathered}
\tag{3}
$$

In Eqs. (1)-(3), $\boldsymbol{\omega}_b = \begin{bmatrix} p & q & r \end{bmatrix}^T$ is the angular velocity vector of the body reference frame (BRF) with respect to the inertial reference frame (IRF); $\mathbf{V}_b = \begin{bmatrix} u & v & w \end{bmatrix}^T$ is the velocity vector of the body axis system origin O with respect to the IRF; the skew-symmetric operator, $\widetilde{(\bullet)}$ or $\mathrm{skew}\left(\bullet\right)$, denotes the matrix-form of the vector cross product; m is the aircraft total mass; $\mathbf{s}_{CG,b}$

refers to the CG position vector in the undeformed (unstrained) condition; $\mathbf{d}_{CG,b} = \mathbf{D}_{CG,b}\mathbf{u}_G$ stands for the change in $\mathbf{s}_{CG,b}$ due to structural deformation; $\mathbf{J}_{O,b}$ is the inertia matrix about O, with respect to the body axes; $\Delta\mathbf{J}'_{O,b}$ is the change in the inertia matrix due to structural deformation; $\mathbf{M}_{GG}$, $\mathbf{B}_{GG}$, and $\mathbf{K}_{GG}$ are the FEM model mass, damping and stiffness matrices, respectively; $\mathbf{F}_b$ and $\mathbf{M}_{O,b}$ are the net force and moment vectors, respectively, associated with the rigid airframe; $\Delta\mathbf{F}_b$ and $\Delta\mathbf{M}_{O,b}$ are the net incremental force and moment vectors, respectively, due to elastic motion; $\mathbf{g}_b$ is the gravity vector expressed in the body axes; $\mathbf{Q}_G$ is the column matrix of generalized aerodynamic and propulsive forces; at last, $\mathbf{M}_{\boldsymbol{\omega}G}$ is the inertial coupling matrix between the rotational rigid-body and the elastic DOFs. The total number of elastic DOFs is n. The notation $\mathbf{e}_{N,i}$ represents a column matrix equal to the ith column of the identity matrix of size N, $\mathbf{I}_N$. All time derivatives are taken in the BRF and no aircraft mass variation is considered.

A structural-dynamic FEM model of the aircraft with lumped properties of inertia is considered available. The n elastic DOFs of the aircraft structure constitute the displacement vector $\mathbf{u}_G = \begin{Bmatrix} u_1 & u_2 & \cdots & u_n \end{Bmatrix}^T$. The transformation matrix $\mathbf{C}_{b0}$ from the inertial axes to the body axes is obtained by a classical sequence (3-2-1) of Euler rotations, ψ, θ and ϕ [13].

The body axes are dually-constrained axes (DCA) [3]. In the DCA, the origin S of the structural axes (the support point, with no elastic displacement) is a material point (and structural node) that can be noncoincident with the origin O of the body axes. Details of the constraint equations for the DCA can be found in Refs. [3, 7]. Any structural node can have its displacements assumed null in the formulation, and the origin O keeps its position constant with respect to the undeformed aircraft (first constraint) and the structural node S is the point where the undeformed and the deformed airframes coincide at any time instant (second constraint).

2.1 Basic aerodynamic model

In this paper, the aerodynamic loads are calculated with the use of the VLM [9], which provides the following linear system of equations:

$$\mathbf{A}^{-1}\Delta\mathbf{C}_\mathbf{p} = \mathbf{w}, \tag{4}$$

where $\mathbf{w} \in \mathbb{R}^{N_P}$ is the vector of non-dimensional normalwashes at the N_P panel (box) control points; $\Delta\mathbf{C}_\mathbf{p} \in \mathbb{R}^{N_P}$ is the vector of panel pressure coefficient differences; and $\mathbf{A} \in \mathbb{R}^{N_P \times N_P}$ is the AIC (aerodynamic influence coefficient) matrix. The VLM AIC matrix depends on the geometry and discretization of the aerodynamic lifting surfaces in the model. Dependence on the Mach number, M, is neglected in this paper.

The body frame of reference used to calculate the aerodynamic loads is defined as an aerodynamic reference frame (ARF) [3]. Its inertial angular rates are written in the ARF coordinate system as p_a, q_a, and r_a, and its inertial velocity has the components u_a, v_a, and w_a in the same system [3]. The rigid-body motion of the aircraft then contributes to the generalized aerodynamic forces (GAFs) in the elastic DOFs in terms of p_a, q_a, r_a, u_a, v_a, w_a, control surface deflections and other possible rigid-body variables. The elastic deformation of the structure with respect to the ARF, given by $\mathbf{u}_{G/A}$, contributes to the incremental GAFs. The total GAFs are then given by [3]:

$$\mathbf{Q}_G = \bar{q}\mathbf{G}_{AG}{}^T\mathbf{S}_{AP}\left(\Delta\mathbf{C}_{\mathbf{p,u}} + \Delta\mathbf{C}_{\mathbf{p,e}}\right), \tag{5}$$

where $\bar{q}$ is the dynamic pressure; $\mathbf{G}_{AG} \in \mathbb{R}^{N_A \times n}$ is the matrix that interpolates elastic displacements from the structural nodes to the centroids of the VLM boxes (aerodynamic grid points);

$\mathbf{S}_{AP} \in \mathbb{R}^{N_A \times N_P}$ transforms panel pressure coefficient differences to forces and moments at the aerodynamic grid points, and is usually called an integration matrix; $\Delta\mathbf{C_{p,u}}$ is the vector of panel pressure coefficient differences related to the rigid-body state and control variables; and $\Delta\mathbf{C_{p,e}}$ is the vector of panel incremental pressure coefficient differences, due to the elastic DOFs, given by [3]:

$$\Delta\mathbf{C_{p,e}} = \mathbf{A}\left(\mathbf{D}_{PA,0}\mathbf{G}_{AG}\mathbf{u}_{G/A} + \left(b_w/V_a\right)\mathbf{D}_{PA,1}\mathbf{G}_{AG}\dot{\mathbf{u}}_{G/A}\right), \tag{6}$$

where $\mathbf{D}_{PA,0}, \mathbf{D}_{PA,1} \in \mathbb{R}^{N_P \times N_A}$ are the differentiation matrices that allow the calculation of control point normalwashes at three quarters of the boxes' mean chords from the displacements at the aerodynamic grid points, respectively; b_w is the reference wing semi-chord; and $N_A = 2N_P$ is the total number of aerodynamic degrees of freedom (each panel has two DOFs, plunge and pitch). The displacement vector $\mathbf{u}_{G/A}$ differs from $\mathbf{u}_G$ in that the former is calculated with respect to the ARF, whereas the latter is with respect to the BRF [3]. The integration and differentiation matrices in Eqs. (5)-(6) can be found in Ref. [7].

In this paper, the ARF is modeled with attached axes [3], and their origin A coincides with or is rigidly connected to a material point C that remains fixed when elastic deformation occurs. References [3, 7] present the equations for the aerodynamic loads based on the ARF DOFs. Induced drag effects due to both the rigid-body motion and the elastic deformations are included, calculated with the methodology of Ref. [14].

2.2 Geometrically-linear beam finite elements

The adopted geometrically-linear beam finite element in three dimensions has two nodes and twelve DOFs. The element shape functions are given by:

$$u_e\left(x_e, y_e, z_e\right) = a_0 + a_1 x_e - \frac{\partial w_e}{\partial x_e} z_e - \frac{\partial v_e}{\partial x_e} y_e, \tag{7}$$

$$v_e\left(x_e, y_e, z_e\right) = \sum_{i=0}^{3} b_i {x_e}^i - \Theta_e\left(x_e, y_e, z_e\right) z_e, \tag{8}$$

$$w_e\left(x_e, y_e, z_e\right) = \sum_{i=0}^{3} c_i {x_e}^i + \Theta_e\left(x_e, y_e, z_e\right) y_e, \tag{9}$$

where $u_e\left(x_e, y_e, z_e\right)$ is the axial displacement and $v_e\left(x_e, y_e, z_e\right)$ and $w_e\left(x_e, y_e, z_e\right)$ are the edgewise and flatwise displacements' shape functions, respectively. The set becomes complete with the twist angle shape function:

$$\Theta_e\left(x_e, y_e, z_e\right) = d_0 + d_1 x_e. \tag{10}$$

The twelve DOFs of the beam element are: at $x_e = y_e = z_e = 0$: $u_e = u_{e1}$, $v_e = v_{e1}$, $w_e = w_{e1}$, $\Theta_e = \phi_{e1}$, $\frac{\partial w_e}{\partial x_e} = -\theta_{e1}$, $\frac{\partial v_e}{\partial x_e} = \psi_{e1}$; at $x_e = L_e, y_e = z_e = 0$: $u_e = u_{e2}$, $v_e = v_{e2}$, $w_e = w_{e2}$, $\Theta_e = \phi_{e2}$, $\frac{\partial w_e}{\partial x_e} = -\theta_{e2}$, and $\frac{\partial v_e}{\partial x_e} = \psi_{e2}$, where L_e is the element length. Strains are given by:

$$\epsilon_x = \frac{\partial u_e}{x_e}, \tag{11}$$

$$\epsilon_y = -\nu\epsilon_x, \tag{12}$$

$$\epsilon_z = -\nu\epsilon_x, \tag{13}$$

$$\gamma_{xy} = \frac{\partial v_e}{x_e} + \frac{\partial u_e}{y_e}, \tag{14}$$

$$\gamma_{xz} = \frac{\partial w_e}{x_e} + \frac{\partial u_e}{z_e}, \tag{15}$$

$$\gamma_{yz} = \frac{\partial w_e}{y_e} + \frac{\partial v_e}{z_e}, \tag{16}$$

where ν is the material Poisson's ratio. Using Voigt's notation, the element strains may be collected in a six-dimensional column matrix, $\boldsymbol{\epsilon} = \left\{\epsilon_x \quad \epsilon_y \quad \epsilon_z \quad \gamma_{xy} \quad \gamma_{xz} \quad \gamma_{yz}\right\}^T$, which is itself a linear function of the twelve element DOFs. Stresses can be calculated with consideration of the isotropic linear elastic material stiffness matrix, $\mathbf{C}$, presented in Ref. [7], so that:

$$\boldsymbol{\sigma} = \mathbf{C}\boldsymbol{\epsilon}. \tag{17}$$

The element stiffness matrix $\mathbf{K}_{ee}$ is such that the element strain energy satisfies:

$$U_e = \frac{1}{2}\iiint\limits_{element} \boldsymbol{\sigma}^T \boldsymbol{\epsilon} dV = \frac{1}{2}\mathbf{u}_e{}^T \mathbf{K}_{ee}\mathbf{u}_e, \tag{18}$$

with $\mathbf{u}_e = \left\{u_{e1} \quad v_{e1} \quad w_{e1} \quad \phi_{e1} \quad \theta_{e1} \quad \psi_{e1} \; u_{e2} \quad v_{e2} \quad w_{e2} \quad \phi_{e2} \quad \theta_{e2} \quad \psi_{e2}\right\}^T$. The final equation for the stiffness matrix is presented in Ref. [7] and is omitted here for brevity.

Although a consistent mass matrix can also be obtained for the beam element, the flight-dynamic formulation is not prepared to deal with consistent masses, due to resulting inertial coupling between the two element nodes. Rather, a lumped-mass matrix is generated by transferring to each node half of the mass of the element, as well as the first and second moments of inertia and the products of inertia due to each half.

2.3 Geometrically-nonlinear formulation

In this paper, the strain-based geometrically-nonlinear (GN) formulation is based on Refs. [15–18]. A toolbox named ITA/AeroFlex was developed with this formulation, using MATLAB® [19]. The formulation considers the following fundamental kinematic relationship that relates the displacements $h(s,t)$ at a point along the beam to the strains $\epsilon(s,t)$:

$$\frac{\partial h}{\partial s}(s,t) = \mathcal{K}(s,t)h(s,t)\,, \tag{19}$$

$$\mathcal{K}(s,t) = \begin{bmatrix} 0 & 1+\epsilon_x(s,t) & 0 & 0 \\ 0 & 0 & \kappa_z(s,t) & -\kappa_y(s,t) \\ 0 & -\kappa_z(s,t) & 0 & \kappa_x(s,t) \\ 0 & \kappa_y(s,t) & -\kappa_x(s,t) & 0 \end{bmatrix}, \tag{20}$$

where $\epsilon_x(s,t)$ is the extensional strain, and $\kappa_x(s,t)$, $\kappa_y(s,t)$ and $\kappa_z(s,t)$ are the curvatures at point s and time t.

The flexible structure is split into elements and the strains are assumed to be spatially-constant but time-dependent along each element, so that Eq. (19) has an analytical solution:

$$h(s,t) = e^{\mathcal{K}(s-s_0)}h_0(t)\,, \tag{21}$$

where $h_0(t)$ is the displacement of a fixed node at $s = s_0$. The matrix exponential $e^{\mathcal{K}(s-s_0)}$ has a closed-form expression, as presented in Ref. [16].

In the ITA/AeroFlex computer program, flexible elements with three nodes were implemented, as well as rigid elements with time-independent, null strain. Such rigid elements are used to model rigid components and do not introduce new states within the model.

Using Eq. (21), it is possible to compute the displacement vector for each structural node as a function of the strains:

$$h(t) = h\left(\epsilon(t)\right) . \tag{22}$$

The time derivative of the displacement vector due to both the strain rates $\dot{\epsilon}$ and the rigid-body motion β (linear and angular velocity components) is given by:

$$\dot{h}(t) = J_{h\epsilon}\dot{\epsilon}(t) + J_{hb}\beta(t) , \tag{23}$$

where $J_{h\epsilon}(\epsilon(t))$ is a Jacobian matrix that relates the element strains to nodal displacements and J_{hb} is the equivalent but for the rigid-body motion.

The kinetic energy is computed as:

$$T = \frac{1}{2}\dot{h}^T M \dot{h} , \tag{24}$$

where M is the structure mass matrix, computed assuming a linear variation of the nodal speeds between the nodes. The kinetic energy can be rewritten as a function of the strain rates and rigid-body velocities using Eq. (23):

$$T = \frac{1}{2}\begin{bmatrix}\dot{\epsilon} & \beta\end{bmatrix}\begin{bmatrix}M_{FF} & M_{FB} \\ M_{BF} & M_{BB}\end{bmatrix}\begin{bmatrix}\dot{\epsilon} \\ \beta\end{bmatrix} , \tag{25}$$

where:

$$\begin{aligned} M_{FF} &= J_{h\epsilon}^T M J_{h\epsilon} , \quad & M_{FB} &= J_{h\epsilon}^T M J_{hb} , \\ M_{BF} &= J_{hb}^T M J_{h\epsilon} , \quad & M_{BB} &= J_{hb}^T M J_{hb} . \end{aligned} \tag{26}$$

The elastic strain energy is given by:

$$U = \frac{1}{2}\epsilon^T K \epsilon , \tag{27}$$

where K is a block-diagonal matrix, composed of the stiffness matrices of each element, K^e:

$$K^e = \begin{bmatrix} k_{11} & k_{12} & k_{13} & k_{14} \\ k_{21} & k_{22} & k_{23} & k_{24} \\ k_{31} & k_{32} & k_{33} & k_{34} \\ k_{41} & k_{42} & k_{43} & k_{44} \end{bmatrix} . \tag{28}$$

From the Euler-Lagrange equations, the equations of motion are computed as:

$$\begin{bmatrix}M_{FF} & M_{FB} \\ M_{BF} & M_{BB}\end{bmatrix}\begin{bmatrix}\ddot{\epsilon} \\ \dot{\beta}\end{bmatrix} + \begin{bmatrix}C_{FF} & C_{FB} \\ C_{BF} & C_{BB}\end{bmatrix}\begin{bmatrix}\dot{\epsilon} \\ \beta\end{bmatrix} + \begin{bmatrix}K \\ 0\end{bmatrix}\epsilon = \begin{bmatrix}R_F \\ R_B\end{bmatrix} , \tag{29}$$

The matrices C_{FF}, C_{BF}, C_{FB} and C_{BB} include the gyroscopic terms (due to rotation of the rigid body and of the structural elements) and the structural damping term. In this paper, the structural damping matrix is assumed proportional to the stiffness matrix: $C_{FF} = \alpha K$.

R_F and R_B are the generalized forces that are applied to the airplane. They are obtained from the aerodynamic, gravitational and propulsive forces applied to each node of the structure:

$$\begin{bmatrix} R_F \\ R_B \end{bmatrix} = \begin{bmatrix} J_{p\epsilon}^T \\ J_{pb}^T \end{bmatrix} F^{pt} + \begin{bmatrix} J_{\theta\epsilon}^T \\ J_{\theta b}^T \end{bmatrix} M^{pt} \tag{30}$$
$$+ \begin{bmatrix} J_{p\epsilon}^T \\ J_{pb}^T \end{bmatrix} B^F F^{dist} + \begin{bmatrix} J_{\theta\epsilon}^T \\ J_{\theta b}^T \end{bmatrix} B^F M^{dist} + \begin{bmatrix} J_{p\epsilon}^T \\ J_{pb}^T \end{bmatrix} N\vec{g}.$$

The Jacobian matrices $J_{p\epsilon}$ and $J_{\theta\epsilon}$ represent the relationship between structural strains (ϵ) and nodal displacements and rotations. J_{pb} and $J_{\theta b}$ represent the relationship between rigid-body DOFs and nodal displacements and rotations. The Jacobian matrices are nonlinear functions of the strain vector ϵ. Closed-form expressions for the Jacobians are presented in Ref. [16].

The aerodynamic loads in the GN formulation are also calculated with a VLM [9] model. However, differently from the GL case, the aerodynamic mesh is updated in the GN formulation to match the deformation of the lifting surfaces in bending.

3 ENHANCED AERODYNAMIC MODEL

This paper aims at the development and numerical test of an enhanced aerodynamic model for the GL formulation that allows it to take into account geometrically-nonlinear aerodynamic effects. It is important to distinguish structural geometrical nonlinearities from aerodynamic geometrical nonlinearities. Structural geometrical nonlinearities refer to how large deformations affect the deformed shape of the structure, as well as its stiffness and inertia properties. Aerodynamic geometrical nonlinearities refer to how even small deformations can affect the aerodynamics of an aircraft in a nonlinear form. For example, the basic aerodynamic model described in Section 2.1 is unable to capture the effects of wing dihedral change due to wing bending, because the VLM mesh is always that of the undeformed aircraft in this basic model.

To illustrate an aerodynamic geometrical nonlinearity, the six-meter-span X-HALE aircraft [7, 8, 12], henceforth named ‘XH6’, is shown in its undeformed and deformed shapes in Figs. 1 and 2, respectively. Particularly, the VLM mesh is shown in both cases, having it been updated in the latter. The deformed case is for trimmed level flight at 17 m/s, 700 m altitude in the ISA (International Standard Atmosphere). The structural deformation was calculated with the GN structural-dynamic model exactly as implemented in Ref. [8]. The wing tip vertical displacement is 12.6% of the wing semi-span. Therefore, in this case, the assumption of small deformations is not violated from the viewpoint of the structural-dynamic model.

Table 1 shows how the aerodynamic side force and rolling moment coefficients’ derivatives with respect to the sideslip angle, C_{Y_β} and C_{l_β}, respectively, are affected by the deformation of the aerodynamic mesh. The lift coefficient derivative with respect to the angle of attack, C_{L_α}, is listed as well. At last, also listed are the Frobenius norms of the AIC matrices for both cases. The mesh deformation results in a configuration with higher dihedral angle, significantly affecting the lateral-directional stability derivatives and reducing the lift coefficient that the configuration generates for the same angle of attack. However, it is also demonstrated that the AIC matrix is practically unaffected by the mesh deformation.

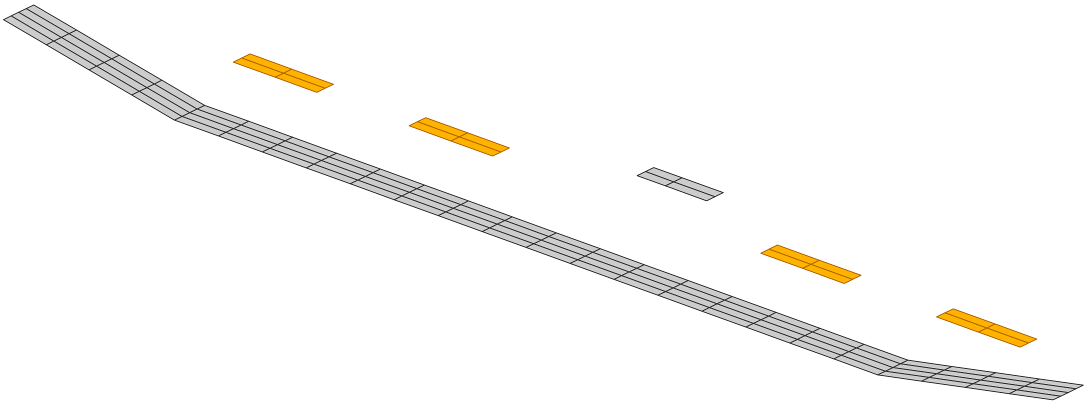

Figure 1: X-HALE six-meter-span configuration VLM mesh in the undeformed condition. Control surfaces in orange.

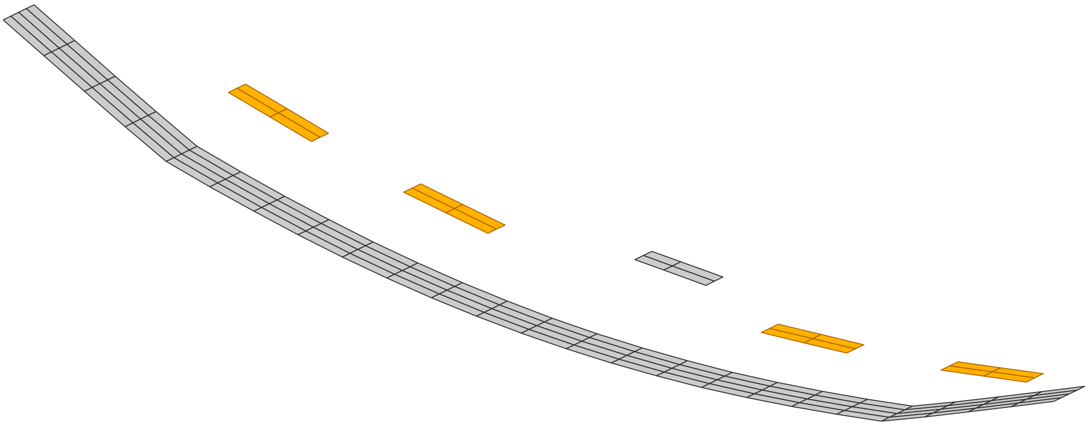

Figure 2: X-HALE six-meter-span configuration updated VLM mesh corresponding to the deformed airframe at $V = 17$ m/s.

Table 1: Aerodynamic characteristics of the X-HALE undeformed and deformed VLM meshes.

VLM Mesh	C_{Y_β} [1/rad]	C_{l_β} [1/rad]	C_{L_α} [1/rad]	$\|\|\mathbf{A}\|\|_F$
Undeformed (Fig. 1)	0.0459	-0.114	6.59	46.446
Deformed (Fig. 2)	0.270	-0.346	6.35	46.467

This example demonstrates that aerodynamic geometrical nonlinearities can occur at levels of structural deformations for which the assumption of small deformations is still valid. Therefore, an enhancement can be made to the aerodynamic model used in the GL formulation to take into account geometrically-nonlinear aerodynamic effects. More interestingly, Table 1 suggests that updating the AIC matrix is potentially unnecessary. The reason for this is that the stronger mutual influences occur among adjacent boxes. Therefore, if the aerodynamic mesh is not absurdly coarse, the local geometry is only very slightly affected by small or even by moderate deformations.

The correction of the normal directions of the boxes, resulting in the aerodynamic normal forces behaving as follower forces, is the first enhancement that is needed to allow the aerodynamic model to capture nonlinear effects like shown in Table 1. This can be done with the modification of the spline matrices, as described in the following subsection.

3.1 Modification of the spline matrices

The procedure will be exemplified for infinite-plate surface splines [2, 20]. The surface spline problem is that of determining deflections $h(x, y)$ when h is known for a discrete set of N_s points, $h_s = h(x_s, y_s)$. The surface spline equation is given by:

$$h(x, y) = a_0 + a_1 x + a_2 y + \sum_{s=1}^{N_s} P_s K_s(x, y), \tag{31}$$

with $K_s(x, y) = c r_s^2 \log(r_s^2)$; $r_s^2 = (x - x_s)^2 + (y - y_s)^2$; c an arbitrary constant; and P_s a scalar varying for each (x_s, y_s), satisfying the conditions:

$$\sum_{s=1}^{N_s} P_s = \sum_{s=1}^{N_s} x_s P_s = \sum_{s=1}^{N_s} y_s P_s = 0. \tag{32}$$

Equations (31) and (32) can then be applied to the N_s known solutions $h_s = h(x_s, y_s)$. As a result, the following matrix equation can be formed:

$$\begin{bmatrix} 0 & 0 & 0 & 1 & \cdots & 1 \\ 0 & 0 & 0 & x_1 & \cdots & x_{N_s} \\ 0 & 0 & 0 & y_1 & \cdots & y_{N_s} \\ 1 & x_1 & y_1 & 0 & \cdots & K_{N_s}(x_1, y_1) \\ \vdots & \vdots & \vdots & \vdots & \ddots & \vdots \\ 1 & x_{N_s} & y_{N_s} & K_1(x_{N_s}, y_{N_s}) & \cdots & 0 \end{bmatrix} \begin{bmatrix} a_0 \\ a_1 \\ a_2 \\ P_1 \\ \vdots \\ P_{N_s} \end{bmatrix} = \begin{bmatrix} 0 \\ 0 \\ 0 \\ h_1 \\ \vdots \\ h_{N_s} \end{bmatrix},$$

$$\mathbf{C_{spline}} \mathbf{p} = \mathbf{h}. \tag{33}$$

The $\mathbf{C_{spline}}$ matrix is symmetric and is non-singular unless one of the N_s points coincides with another or unless all the points are contained in a single straight line. The coordinate system considered for (x, y) is a coordinate system s in which the xy plane (the spline plane) lies in the plane of the lifting surface, the x axis is parallel to the x axis of the coordinate system m in which the VLM/DLM mesh is defined, and the z axis is such that $\hat{z}_s \cdot \hat{z}_m \geq 0$.

Each known displacement h_i normal to the spline plane can be expressed in the following manner:

$$h_i = \mathbf{e}_{3,3}^T \mathbf{C}_{sb} \mathbf{U}_{t,i,G} \mathbf{u}_G. \tag{34}$$

The known displacements are those of a selected set of N_s structural nodes. The matrix $\mathbf{C}_{sb}$ transforms from the body coordinate system to the spline coordinate system. The Boolean matrix $\mathbf{U}_{t,i,G}$ recovers from the structural displacement vector $\mathbf{u}_G$ the translational displacements of the ith spline node.

The enhanced methodology described in this paper then proposes an on-line update of the $\mathbf{C}_{sb}$ matrices in flight simulations of flexible aircraft. With the deformation of the lifting surface, the local dihedral angle changes, and so does the y and z directions of the spline coordinate system s. It is implicit in this methodology that each strip of VLM/DLM boxes (panels) in a lifting surface shall then have its own spline, because the dihedral of any individual strip will change in the deformed aircraft.

The procedure that was just described for a surface spline can be analogously implemented for a linear spline as well. Generally, aeroelastic models of aircraft will have both types of splines.

3.2 Corrected rigid-body aerodynamics

Once the spline matrix is updated, but the aerodynamic model geometry is not, a technique to calculate the rigid-body aerodynamic loads needs to be developed. Otherwise, nonlinear effects like those contained in Table 1 will not be represented in the rigid-body DOFs EOMs, Eqs. (1) and (2).

Because the FEM model stiffness matrix $\mathbf{K}_{GG}$ is for the unrestrained aircraft, it is possible to obtain six rigid-body modes from it, as in Ref. [3]. Then, let the rigid-body mode matrix about the origin of the ARF, A, be represented by $\mathbf{\Psi}_{r,A}$. If $\mathbf{Q}_G$ is the vector of GAFs in the elastic DOFs, given by an equation similar to Eq. (5), but with the original undeformed spline matrix $\mathbf{G}_{AG}$ replaced by modified one, $\mathbf{G}_{AG}^{def}$, then the GAFs in the rigid-body DOFs can be calculated by the equation:

$$\mathbf{Q}_{RB} = \mathbf{\Psi}_{r,A}^T \mathbf{Q}_G = \bar{q} \mathbf{\Psi}_{r,A}^T \mathbf{G}_{AG}^{def^T} \mathbf{S}_{AP} \left(\Delta \mathbf{C}_{\mathbf{p},\mathbf{u}} + \Delta \mathbf{C}_{\mathbf{p},\mathbf{e}} \right). \tag{35}$$

The first three components of $\mathbf{Q}_{RB}$ are the corrected forces in the three body axes directions, whereas the other three components are the corrected moments about A in the three body axes directions.

3.3 Further enhancement of the aerodynamic model

The correction of the spline planes to match the deformed dihedral of the lifting surface makes possible both the correction of the amplitudes of the normalwashes at the boxes, through the use of the modified spline matrix $\mathbf{G}_{AG}^{def}$ in Eq. (6), and the correction of the GAFs amplitudes in both the rigid-body DOFs and the elastic DOFs, as seen in Eq. (35).

However, one important effect is not yet captured solely by the spline modification. If the lifting surfaces have their planes updated in the spline construction, it is implicit that they do not anymore coincide with the undeformed structural-dynamic model. Because the undeformed structural-dynamic model continues to be valid throughout the flight simulation using the GL formulation, the mismatch between the spline planes and the corresponding structural nodes needs to be taken into account. Particularly, the aerodynamic normal force acting at the quarter-chord point at half the box span produces a bending moment at the structural nodes used in the corresponding spline definition, because of the relative displacement between the spline plane and the original structural node position. These additional nonlinear generalized forces can be calculated as follows:

$$\Delta \mathbf{Q}_x = \bar{q} \mathbf{U}_{r,x}^T \left(diag \left(\mathbf{U}_{t,y} \mathbf{u}_{G/A} \right) \mathbf{U}_{t,z}^T - diag \left(\mathbf{U}_{t,z} \mathbf{u}_{G/A} \right) \mathbf{U}_{t,y}^T \right) \mathbf{G}_{AG}^{def^T} \mathbf{S}_{AP} \Delta \mathbf{C}_{\mathbf{p}}, \tag{36}$$

$$\Delta \mathbf{Q}_y = \bar{q} \mathbf{U}_{r,y}^T \left(diag \left(\mathbf{U}_{t,z} \mathbf{u}_{G/A} \right) \mathbf{U}_{t,x}^T - diag \left(\mathbf{U}_{t,x} \mathbf{u}_{G/A} \right) \mathbf{U}_{t,z}^T \right) \mathbf{G}_{AG}^{def^T} \mathbf{S}_{AP} \Delta \mathbf{C}_{\mathbf{p}}, \tag{37}$$

$$\Delta \mathbf{Q}_z = \bar{q} \mathbf{U}_{r,z}^T \left(diag \left(\mathbf{U}_{t,x} \mathbf{u}_{G/A} \right) \mathbf{U}_{t,y}^T - diag \left(\mathbf{U}_{t,y} \mathbf{u}_{G/A} \right) \mathbf{U}_{t,x}^T \right) \mathbf{G}_{AG}^{def^T} \mathbf{S}_{AP} \Delta \mathbf{C}_{\mathbf{p}}, \tag{38}$$

where $\Delta \mathbf{Q}_x$, $\Delta \mathbf{Q}_y$, and $\Delta \mathbf{Q}_z$ are the incremental GAFs due to moments about x_b, y_b, and z_b, respectively, produced by the lifting surface deformation; $\mathbf{U}_{t,x}$, $\mathbf{U}_{t,y}$, and $\mathbf{U}_{t,z}$ are the Boolean matrices that select from the displacement vector $\mathbf{u}_G$ the translational displacements in the x_b, y_b, and z_b body axes, respectively; $\mathbf{U}_{r,x}$, $\mathbf{U}_{r,y}$, and $\mathbf{U}_{r,z}$ are the Boolean matrices that select from $\mathbf{u}_G$ the rotational displacements about x_b, y_b, and z_b, respectively; $\Delta \mathbf{C}_{\mathbf{p}} = \Delta \mathbf{C}_{\mathbf{p},\mathbf{u}} + \Delta \mathbf{C}_{\mathbf{p},\mathbf{e}}$; and $diag$ is the operator that creates a diagonal matrix from a column matrix.

In summary, in the final enhanced aerodynamic model, the total GAFs are given by:

$$\mathbf{Q}_G^{enhanced} = \bar{q}\mathbf{E}_n \mathbf{G}_{AG}^{def^T} \mathbf{S}_{AP} \left(\Delta\mathbf{C}_{\mathbf{p,u}} + \Delta\mathbf{C}_{\mathbf{p,e}}\right), \tag{39}$$

$$\begin{aligned}\mathbf{E}_n = \mathbf{I}_n &+ \mathbf{U}_{r,x}^T \left(diag\left(\mathbf{U}_{t,y}\mathbf{u}_{G/A}\right)\mathbf{U}_{t,z}^T - diag\left(\mathbf{U}_{t,z}\mathbf{u}_{G/A}\right)\mathbf{U}_{t,y}^T\right)\\ &+\mathbf{U}_{r,y}^T \left(diag\left(\mathbf{U}_{t,z}\mathbf{u}_{G/A}\right)\mathbf{U}_{t,x}^T - diag\left(\mathbf{U}_{t,x}\mathbf{u}_{G/A}\right)\mathbf{U}_{t,z}^T\right)\\ &+\mathbf{U}_{r,z}^T \left(diag\left(\mathbf{U}_{t,x}\mathbf{u}_{G/A}\right)\mathbf{U}_{t,y}^T - diag\left(\mathbf{U}_{t,y}\mathbf{u}_{G/A}\right)\mathbf{U}_{t,x}^T\right),\end{aligned} \tag{40}$$

$$\Delta\mathbf{C}_{\mathbf{p,e}} = \mathbf{A}\left(\mathbf{D}_{PA,0}\mathbf{G}_{AG}^{def}\mathbf{u}_{G/A} + \left(b_w/V_a\right)\mathbf{D}_{PA,1}\mathbf{G}_{AG}^{def}\dot{\mathbf{u}}_{G/A}\right), \tag{41}$$

and the GAFs in the rigid-body DOFs are:

$$\mathbf{Q}_{RB}^{enhanced} = \mathbf{\Psi}_{r,A}^T \mathbf{Q}_G^{enhanced}. \tag{42}$$

The modified GAFs in the rigid-body DOFs given by Eq. (42) automatically include the moments that exist due to the fact that the moment arms vary with the deformation of the aircraft.

4 NUMERICAL MODEL

The X-HALE aircraft in its six-meter-span ('XH6') configuration is analyzed in this paper. The XH6 configuration contains six wing sections with span of 1.0 m and chord of 0.2 m each, as well as five pods at the connections between wing sections. The aircraft electric motors, landing gears, electronics and sensors are installed at the pods. Booms are connected to the pods and, at the tip of each boom, a horizontal tail is mounted. The four side tails are all-moving control surfaces that can be used for both longitudinal and lateral-directional control, and are then termed elevons. The central tail has a flipping-up capability that alters the aircraft flying qualities as desired in operation. For ground clearance during take-off, the central tail has approximately 33% less span in its right (bottom) part than in the left (top) part. Anyway, the configuration analyzed in this paper has the central tail in the horizontal position. The wing-tip sections have a dihedral angle of 10°. The wing is built with an incidence of 5°.

The numerical model of the nominal aircraft considers exactly the same stiffness properties previously adopted in Refs. [7, 8], and these properties are used in both the GL and the GN formulations. All aircraft components except the wing are assumed rigid. The distributed mass properties of the aircraft components are also identical to those presented in Table 1 of Ref. [7]. The concentrated inertias match those listed in Table 7 of Ref. [12].

4.1 GL and GN models

The objective of this paper is to apply and verify the enhanced aerodynamic model in the GL formulation. For the verification, the GL results will be compared with those obtained with the GN formulation. Hence, it is necessary to ensure that the GL and GN numerical models are adequate for a fair comparison of results.

In the GN formulation, because all structural DOFs are kept in the EOMs, the resulting dynamical system has hundreds of states and its ordinary differential equations (ODEs) are stiff. It was found via numerical tests that the most commonly used ODE solvers, like the fixed-stepsize fourth-order Runge-Kutta or the adaptive-stepsize Dormand-Prince methods, were unable to solve the equations. Instead, the generalized-α algorithm [16, 21, 22] was found able to solve them. Currently, in ITA/AeroFlex, the nonlinear balance equation of this implicit algorithm is solved at each time step with the trust-region dogleg algorithm implemented in the MATLAB® 'fsolve' function. A reduction in the number of structural DOFs is then mandatory to make the simulations less costly.

Having this in mind, it was found in Ref. [8] that using 4 elements per wing section in the GN model and 8 elements in the GL yields no more than 3.5% difference between them with respect to modal frequencies less than 20 Hz. This refinement is coarser than the one used previously in Ref. [7], where the authors were concerned almost only with accuracy of the models in static conditions, with model size having less computational impact because ODEs were not to be solved. There, convergence analyses led to 10 elements per wing section in the GN formulation and 20 in the GL. With either of the choices described in this paragraph, the wing has the same quantity of nodes in both the GN and the GL models. Moreover, a time step of 10 milliseconds is used in numerically solving the ODEs in this paper, rendering differences in higher-frequency modes progressively less important the farther they are from 20 Hz.

The VLM mesh is the same for both formulations and, for the same reasons as the aforementioned ones, is coarser than the one adopted in Ref. [7]. For simplicity, it was built to match the spanwise divisions of the wing sections in the GN structural-dynamic model, that is, it comprises 4 uniformly distributed boxes spanwise per wing section. Chordwise, 4 boxes are used in the wing, also uniformly distributed. The tails are divided into 2 boxes chordwise and 2 boxes spanwise. No vertical surface representing each pod is included in the aerodynamic model, also for simplicity. The VLM mesh is exactly as shown before in Fig. 1.

The wing incidence of $5°$ and the wing reflexed EMX07 airfoil [12] camber are approximately represented by invariant normalwash vectors, given by the local effective camber line inclination at 75% of each box chord.

In the GN formulation, the VLM mesh is updated with structural deformation, such that the wing and tails' boxes' side edges are displaced by exactly the same amount as the structural node with which they coincide spanwise. Whether the AIC matrix is updated or not will be made clear in each of the analyzed cases.

The displacements and velocities of the beam elements' central nodes in the GN formulation are directly used to calculate the normalwashes. No camber deformation is considered, and hence the displacement transferal from the structural nodes to the boxes' control points is straightforward, assuming rigid arms. The aerodynamic loading is considered as distributed, and appropriate matrices transfer the distributed loads to nodal loads at each element, as in Eq. (30).

In the GL formulation, if the enhanced aerodynamic model is not used, then the VLM mesh is always that of the undeformed aircraft; if it is used, then the methodology derived in Section 3 is considered. The GL structural-dynamic model for the XH6 configuration is plotted in Fig. 3.

In the time-marching simulations, stiffness-proportional structural damping is considered both for the GL and the GN formulations, with a constant of proportionality such that the first free-free mode of vibration has 2% damping ratio. In the GL case, the structural displacements are represented by modal coordinates, with inertia-relieved constrained modes of vibration [3] with frequency less than 25 Hz retained in the modal basis. This choice is consistent with the time step of 10 milliseconds used for all simulations shown in this paper.

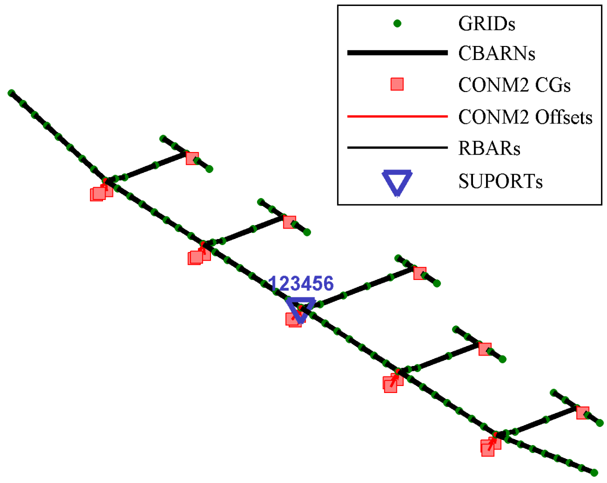

Figure 3: XH6 GL structural-dynamic model in ITA/AeroFlex. GRIDs: structural nodes; CBARNs: beam elements; RBARs: rigid bar elements; CONM2 CGs: CG locations of lumped-mass elements; CONM2 Offsets: offsets between such CG locations and the structural node to which the lumped-mass element is attached; and SUPORT: support location.

5 NUMERICAL RESULTS

In Table 1, it was shown that the Frobenius norm of the AIC matrix was practically insensitive to the airframe deformation in an equilibrium condition of straight level flight, at an airspeed of 17 m/s. Now, it is important to evaluate if this insensitivity is also observed in maneuvering flight.

Time-marching simulations were performed to obtain the aircraft response to an asymmetrical elevon doublet. The doublet lasts 1.2 second and is applied only to the right outboard elevon. The pulses have amplitude of 10.0° and are C1-continuous with cubic transitions lasting 0.2, 0.4 and 0.2 second, respectively. The commands begin at $t = 0.2$ s, with the aircraft initially in a trimmed straight level flight condition with $V = 17$ m/s. The first pulse is positive and the second is negative.

Figure 4 shows that the aircraft pitch rate and roll rate responses to the asymmetrical elevon doublet are practically unaffected by the absence of the AIC matrix update. Figure 5 shows that the maximum vertical displacement occurs at the left wing tip and is about 18.7% of the wing semi-span. This level of deformation is beyond that for which small deformations would still be valid [7, 8]. Therefore, this flight simulation demonstrates that, for the XH6 and for the aerodynamic mesh in use, the AIC matrix update is indeed not necessary. In the the sequence of the paper, whenever the GN formulation is mentioned, results obtained without AIC matrix update will be shown.

Then, we can proceed to the evaluation of the methodology proposed in this paper, which enhances the aerodynamic model used in the GL formulation with both the modification of the spline matrices and with the consideration of additional GAFs due to mismatch between the deformed spline planes and the undeformed structural-dynamic model. A central support location is used in the GL formulation in this paper.

First, results for the equilibrium condition of straight level flight at $V = 17$ m/s are shown in Table 2. In this case, the enhanced model works almost perfectly when compared with the GN formulation, and it is seen that the GL formulation with the enhanced aerodynamic model is

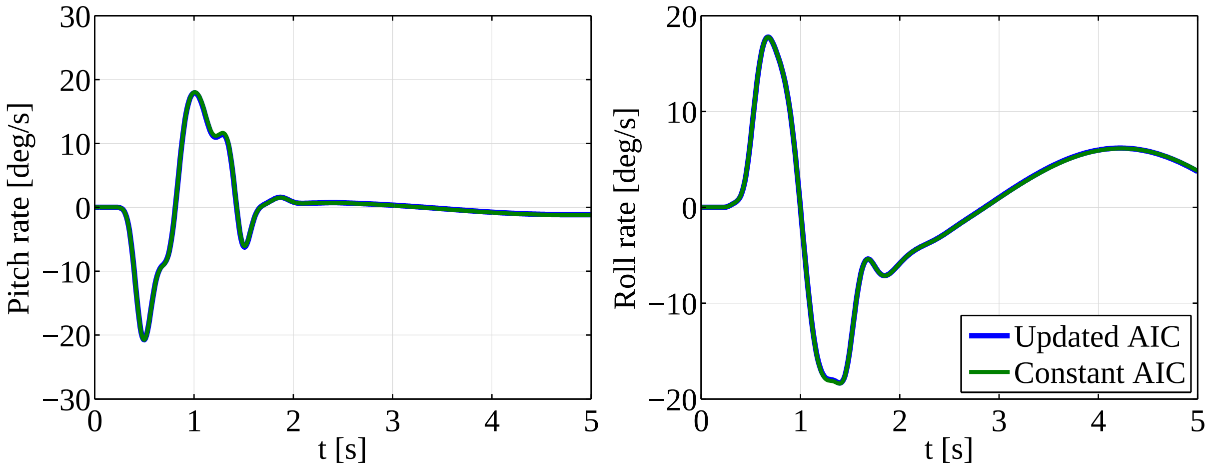

Figure 4: XH6 pitch rate and roll rate responses to asymmetrical elevon doublet at 17 m/s, with and without AIC matrix update.

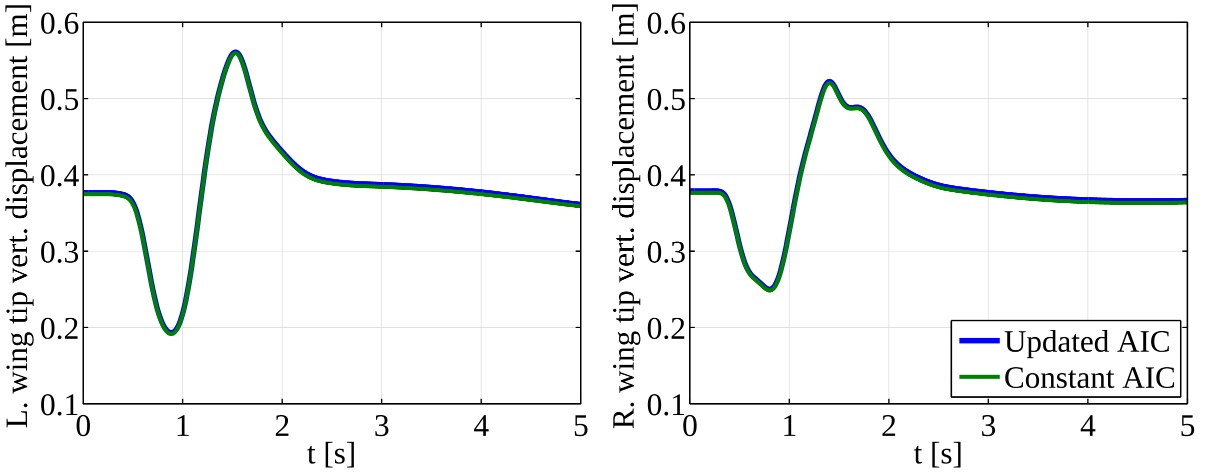

Figure 5: XH6 wing tip vertical displacements in response to asymmetrical elevon doublet at 17 m/s, with and without AIC matrix update.

able to capture the additional bending caused by the aerodynamic forces behaving as follower forces. The wing tip vertical displacement is close to 12.5% of the wing semi-span, which was observed to be the threshold between small and large deformations in previous works [7, 8]. The newly-proposed methodology is able to increase the fidelity of the GL formulation with a much lower computing cost than that necessary in the GN formulation.

Table 2: Wing tip vertical displacements (positive upwards) for the XH6 configuration in trimmed straight level flight at 17 m/s. (Percentages with respect to GN left and right wing tip displacements.)

Wing Tip	Displacements [m] GN	GL (Constant spline)	GL (Enhanced)
Left	0.375	0.310 (-17.3%)	0.377 $(+0.5\%)$
Right	0.377	0.312 (-17.2%)	0.379 $(+0.5\%)$

Table 3 shows other relevant results for the straight level flight at 17 m/s, regarding important stability derivatives of the aircraft. These stability derivatives are obtained by the linearization of the aircraft dynamics about the equilibrium condition, after having properly included the ARF angle of attack, the ARF sideslip angle and all the aerodynamic coefficients in the output vector of the dynamics. The stability derivatives of Table 3 are for the deformed airframe but without quasi-static aeroelastic effects, that is, they are for a rigid aircraft having the shape of the deformed airframe in the equilibrium condition. It is seen that the enhanced GL formulation is much closer to the results obtained with the GN formulation, with the highest relative error of $+2.3\%$ observed for the C_{m_α} derivative. The enhanced GL and the GN formulations have a significantly better agreement with respect to the sideslip angle derivatives. It is then expected that the enhanced GL formulation leads to much better results than the unmodified GL when e.g. the aircraft response to side gusts is analyzed.

Table 3: Stability derivatives for the XH6 configuration in trimmed straight level flight at 17 m/s. (Percentages with respect to GN derivatives.)

Stability Derivative	GN	GL (Constant spline)	GL (Enhanced)
C_{L_α} [1/rad]	6.352	6.590 $(+3.7\%)$	6.353 $(+0.02\%)$
C_{m_α} [1/rad]	-2.956	-2.503 (-15.3%)	-3.023 $(+2.3\%)$
C_{Y_β} [1/rad]	0.268	0.0459 (-82.9%)	0.268 (0.0%)
C_{l_β} [1/rad]	-0.345	-0.114 (-67.0%)	-0.348 $(+0.9\%)$

The results shown in Tables 2 and 3 are for a flight condition in which deformations are near the threshold between small and large deformations, and this explains why the GL formulation with the enhanced aerodynamic model works so well. It is important to show that, for higher levels of deformation, the methodology will naturally stop to produce reliable results, because for higher levels of deformation the structural-dynamic geometrical nonlinearities grow in importance and are not captured by the GL formulation. Such a kind of result is shown in Table 4, for a longitudinal maneuver with vertical load factor of 1.5 at $V = 20$ m/s. The wing tip displacements predicted by the GL formulations either underestimate or overestimate those obtained with the higher-fidelity GN formulation. The wing tip vertical displacement is close to 23.2% of the wing semi-span, clearly in the range of large deformations [7, 8].

Table 4: Wing tip vertical displacements (positive upwards) for the XH6 configuration in trimmed longitudinal flight with a vertical load factor of 1.5 at 20 m/s. (Percentages with respect to GN left and right wing tip displacements.)

Wing Tip	Displacements [m] GN	GL (Constant spline)	GL (Enhanced)
Left	0.692	0.462 (-33.2%)	0.843 $(+21.8\%)$
Right	0.697	0.466 (-33.1%)	0.853 $(+22.4\%)$

Figure 6, which contains the aircraft response to the asymmetrical elevon doublet previously described, shows that the GL formulation with the enhanced aerodynamic model results in pitch rate and roll rate time histories that more closely follow those of the GN formulation. This is because the on-line correction of the local dihedral angles of the lifting surfaces in the enhanced method allows the modification not only of the aircraft response characteristics but of the elevon effectiveness as well. One of the effects is that, because of the wing deformation in bending, the elevon has a smaller arm to produce rolling moment. For the same reason, the same elevon deflection also generates less force in the body z-axis, then producing smaller pitching moment as well. These factors contribute to the smaller magnitudes in the aircraft pitch rate and roll rate responses.

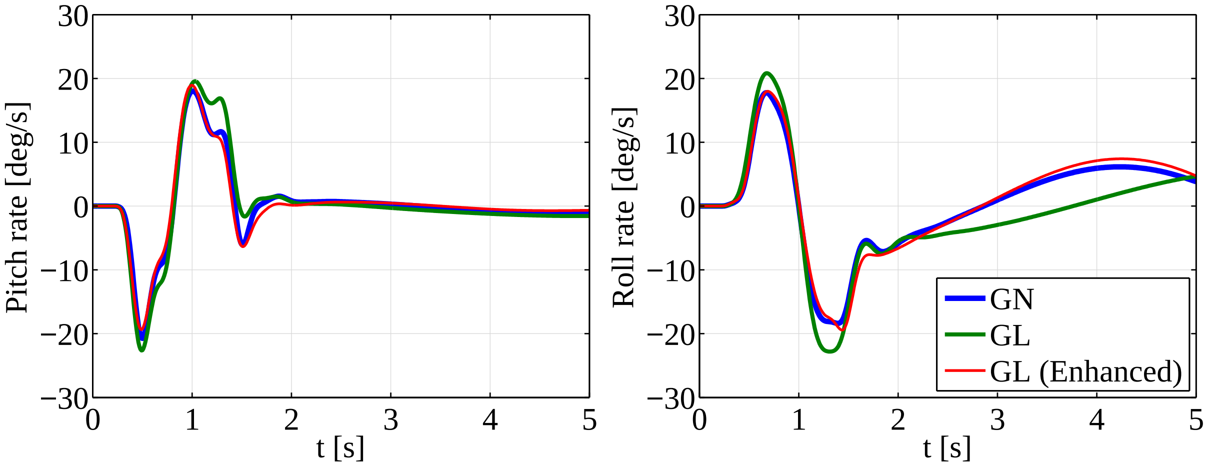

Figure 6: Nominal XH6 ($\sigma = 1$) pitch rate and roll rate responses to asymmetrical elevon doublet at 17 m/s.

The deformations attained in the maneuver, shown in Fig. 7, are large, reaching about 18.7% of the the wing semi-span at the left wing tip in the GN formulation. The GL formulation with the enhanced aerodynamic model more closely follows the time histories of the wing-tip displacements in the GN formulation, but when the largest deformations occur, between 1 and 2 seconds of simulation, the enhanced GL formulation overestimates them. This is because at such levels of deformation the geometrical linearity of the structural-dynamic model is not valid anymore.

Nevertheless, considering that the GL formulation has much lower computing time than the GN (few minutes for the enhanced GL compared with few hours for the GN in a regular desktop computer, for the five-second simulations under analysis), one would generally be satisfied with the low level of disagreement obtained between the GN and the enhanced GL formulations.

It is important to show another case in which the level of deformation attained is smaller. For this, the stiffness matrix of the aircraft is multiplied by a factor σ:

$$\mathbf{K}'_{GG} = \sigma \mathbf{K}_{GG}. \tag{43}$$

Hence, whereas the nominal aircraft analyzed until now has $\sigma = 1$, now we analyze the stiffened aircraft, with $\sigma = 2$. The structural damping is not modified. Figures 8 and 9 show the results of the asymmetrical elevon doublet with $\sigma = 2$. The agreement between the GN and the enhanced GL formulations is even better, validating the methodology proposed in this paper. Two interesting results appear if one carefully compares Figs. 6 and 8. The first is that there is almost no difference in the amplitude of the pitch rate response between these two stiffness

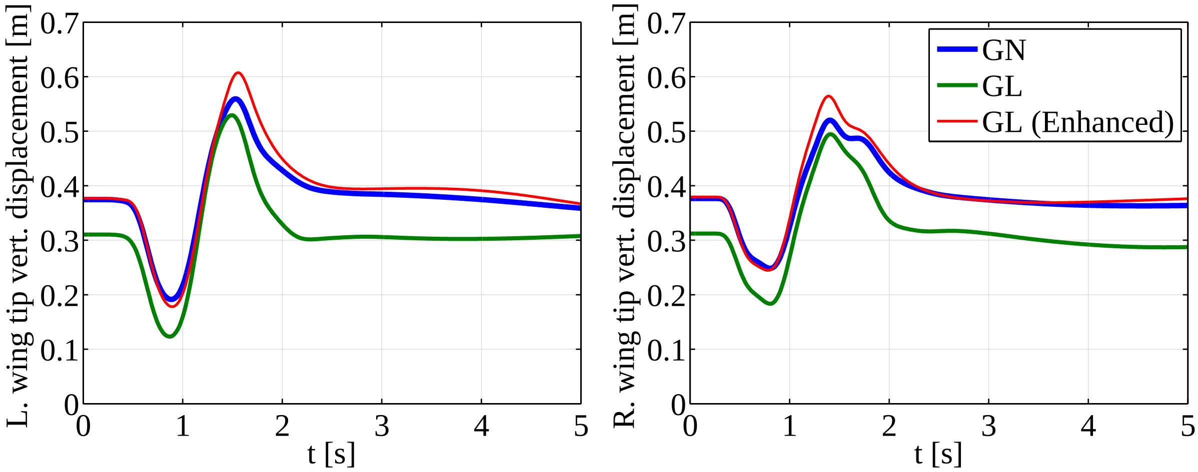

Figure 7: Nominal XH6 ($\sigma = 1$) wing tip vertical displacements in response to asymmetrical elevon doublet at 17 m/s.

levels, indicating that the pitching motion is dominated by the rigid-body dynamics. The second is that, despite the first pulse of the right outer elevon deflection is positive (trailing edge down), the initial roll rate response is positive (right wing down) in both cases, but of much larger amplitude in the nominal aircraft. Actually, the elevon roll control is reversed in the XH6, and its effectiveness in reversal decreases if the stiffness increases.

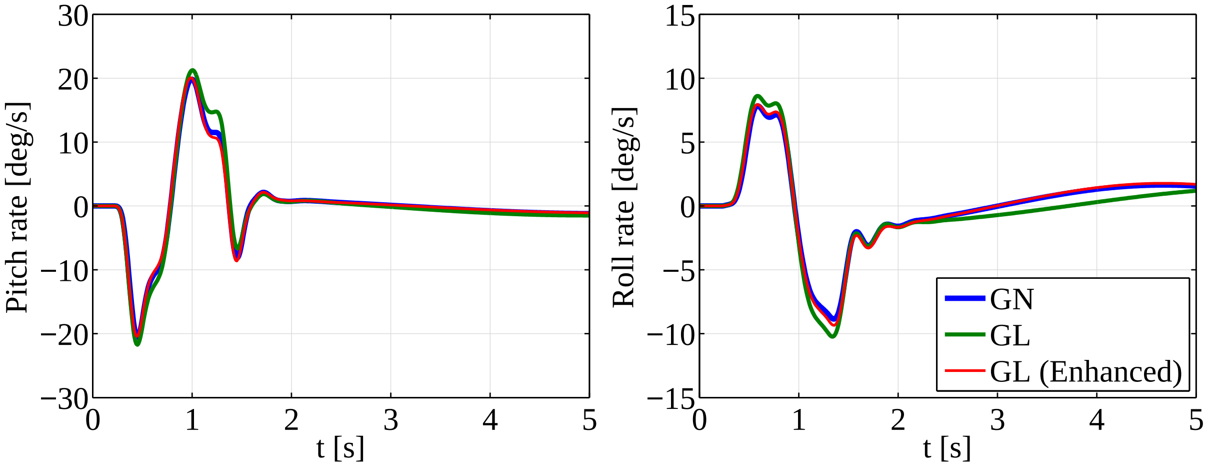

Figure 8: Stiffened XH6 ($\sigma = 2$) pitch rate and roll rate responses to asymmetrical elevon doublet at 17 m/s.

Regarding the geometrical nonlinearities in the structural-dynamic model, one thing that is easily observed in a GL formulation is that, the larger the deformations are, the more stretched the structure becomes, because of the geometrical linearity. To observe this stretching, the total structural length of the wing was calculated in the simulations for $\sigma = 1$ and for $\sigma = 2$. The results are shown in Fig. 10. In the nominal aircraft, the wing structure stretches up to about 0.14 m (2.3% of wing span), whereas in the stiffened aircraft the maximum stretching is about 0.03 m (0.5% of wing span), both in the enhanced GL formulation. Comparatively, the geometrically-nonlinear structure almost does not have its length changed. The structural stretching can be concluded to be the most important limitation of the GL structural-dynamic model. More extensive analysis could even help to derive a criterion for validity of small deformations based on how much the structural length is increased.

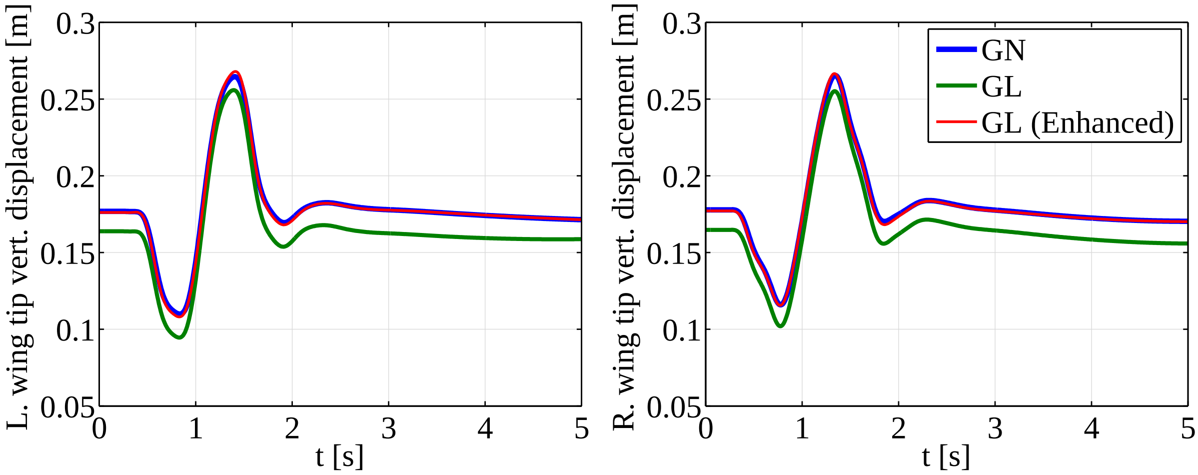

Figure 9: Stiffened XH6 ($\sigma = 2$) wing tip vertical displacements in response to asymmetrical elevon doublet at 17 m/s.

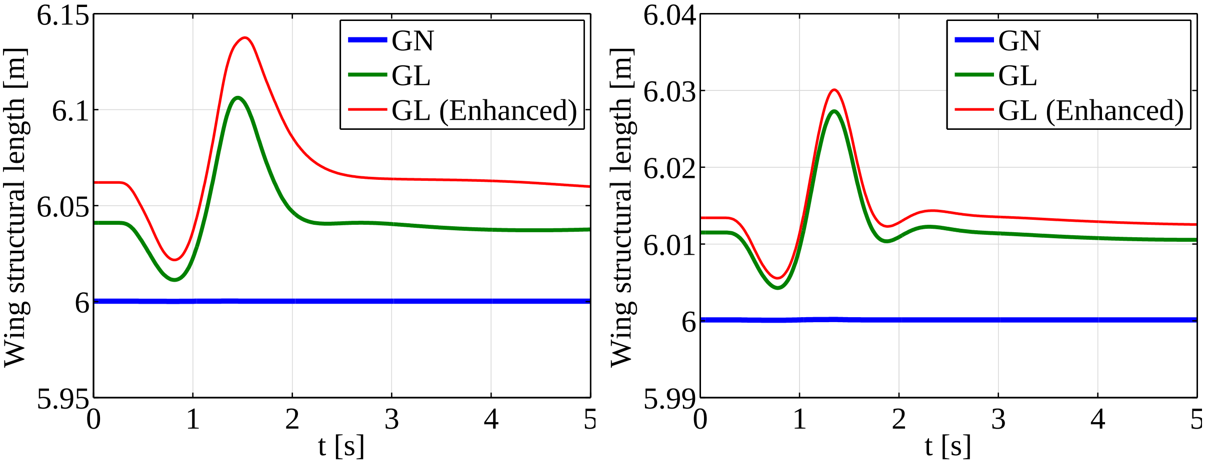

Figure 10: XH6 ($\sigma = 1$ on the left, $\sigma = 2$ on the right) wing structural length in response to asymmetrical elevon doublet at 17 m/s.

6 CONCLUSIONS

In this paper, an enhanced aerodynamic model for geometrically-linear flight dynamics formulations of flexible aircraft was proposed and evaluated. The proposed model includes the effects caused by the deformation in bending of the lifting surfaces on the spline interpolation classically used in geometrically-linear models. Additional generalized aerodynamic forces due to the mismatch between the displaced spline planes and the undeformed aircraft structure are also derived and included in the enhanced model.

The enhanced model as developed was applied to the classical vortex-lattice method in which only lifting surface boxes are included in the model, without any model of the aerodynamic wake. As such, the proposed model is also directly extendable to the doublet-lattice method combined with rational function approximations. Because one of the main findings was that the aerodynamic influence coefficient matrix does not need to be updated on-line during simulation, the extension to the doublet-lattice method would be seamless and without implying the need to recalculate the rational function approximations at each time step.

Comparisons between the geometrically-linear formulation, both with and without the enhanced aerodynamic model, and the geometrically-nonlinear formulation revealed that the enhanced model captures several phenomena that the unmodified model is unable to capture. For example, the stability derivatives due to angle of attack or sideslip angle, which were seen to be significantly affected by the wing bending in a flight condition as simple as straight level flight, are almost exactly calculated by the enhanced model, whereas the unmodified model predicts some very inaccurate values.

Nonlinear simulations of the X-HALE aircraft response to an asymmetrical right outer elevon doublet also demonstrated the potential of the enhanced geometrically-linear model to more closely follow the time histories obtained with the geometrically-nonlinear formulation, with the former needing only a fraction of the computing time of the latter. However, whenever structural-dynamic geometrical nonlinearities occur, the differences between them may grow, as expected. The main factor of inaccuracy in a geometrically-linear structural-dynamic model was seen to be the stretching of the wing structure, which is practically nonexistent in the geometrically-nonlinear model. Further studies can now be made regarding this phenomenon.

7 REFERENCES

[1] Rodden, W. P. and Love, J. R. (1985). Equations of motion of a quasisteady flight vehicle utilizing restrained static aeroelastic characteristics. *Journal of Aircraft*, 22(9), 802–809. doi:10.2514/3.45205.

[2] Rodden, W. P. and Johnson, E. H. (1994). *MSC.NASTRAN Aeroelastic Analysis User's Guide*. MacNeal-Schwendler Corporation, Los Angeles.

[3] Guimarães Neto, A. B., Silva, R. G. A., Paglione, P., and Silvestre, F. J. (2016). Formulation of the flight dynamics of flexible aircraft using general body axes. *AIAA Journal*, 54(11), 3516–3534. doi:10.2514/1.J054752.

[4] Etkin, B. (1959). *Dynamics of Flight: Stability and Control*. New York: John Wiley & Sons, Inc.

[5] Waszak, M. R. and Schmidt, D. K. (1988). Flight dynamics of aeroelastic vehicles. *Journal of Aircraft*, 25(6), 563–571. doi:10.2514/3.45623.

[6] Silvestre, F. J. and Luckner, R. (2015). Experimental validation of a flight simulation model for slightly flexible aircraft. *AIAA Journal*, 53(12), 3620–3636. doi:10.2514/1.J054023.

[7] Guimarães Neto, A. B., Silvestre, F. J., Cardoso-Ribeiro, F. L., Bussamra, F. L. S., Silva, R. G. A., and Cesnik, C. E. S. (2017). Validity of the assumption of small deformations in aircraft with different levels of structural flexibility. In *International Forum on Aeroelasticity and Structural Dynamics (IFASD) 2017*. Como, Italy. IFASD-2017-080.

[8] Guimarães Neto, A. B., Cardoso-Ribeiro, F. L., and Silvestre, F. J. (2018). Applicability of geometrically-linear structural-dynamic models for the flight dynamics of arbitrarily-flexible aircraft. In *31st Congress of the International Council of the Aeronautical Sciences (ICAS) 2018*. Belo Horizonte, Brazil. ICAS2018-0523.

[9] Hedman, S. G. (1965). Vortex lattice method for calculation of quasi steady state loadings on thin elastic wings. Tech. Rep. 105, Aeronautical Research Institute of Sweden, Stockholm.

[10] Albano, E. and Rodden, W. P. (1969). A doublet-lattice method for calculating lift distributions on oscillating surfaces in subsonic flows. *AIAA Journal*, 7(2), 279–285. doi: 10.2514/3.5086.

[11] Eversman, W. and Tewari, A. (1991). Consistent rational function approximation for unsteady aerodynamics. *Journal of Aircraft*, 29(9), 545–552. doi:10.2514/3.46062.

[12] Cesnik, C. E. S., Senatore, P. J., Su, W., Atkins, E. M., and Shearer, C. M. (2012). X-HALE: A very flexible unmanned aerial vehicle for nonlinear aeroelastic tests. *AIAA Journal*, 50(12), 2820–2833. doi:10.2514/1.J051392.

[13] Stevens, B. and Lewis, F. (2003). *Aircraft Control and Simulation*. Wiley. ISBN 9780471371458.

[14] Kálmán, T. P., Giesing, J. P., and Rodden, W. P. (1970). Spanwise distribution of induced drag in subsonic flow by the vortex lattice method. *Journal of Aircraft*, 7(6), 574–576. doi:10.2514/3.44219.

[15] Brown, E. L. (2003). *Integrated strain actuation in aircraft with highly flexible composite wings*. Ph.D. thesis, Massachusetts Institute of Technology, Cambridge, MA. PhD in Mechanical Engineering.

[16] Shearer, C. M. (2006). *Coupled nonlinear flight dynamics, aeroelasticity and control of very flexible aircraft*. Ph.D. thesis, University of Michigan, Ann Arbor. PhD in Aerospace Engineering.

[17] Su, W. (2008). *Coupled nonlinear aeroelasticity and flight dynamics of fully flexible aircraft*. Ph.D. thesis, University of Michigan, Ann Arbor. PhD in Aerospace Engineering.

[18] Su, W. and Cesnik, C. E. S. (2011). Strain-based geometrically nonlinear beam formulation for modeling very flexible aircraft. *International Journal of Solids and Structures*, 48(16-17), 2349–2360. doi:10.1016/j.ijsolstr.2011.04.012.

[19] Cardoso-Ribeiro, F. L., Paglione, P., Silva, R. G. A., and Sousa, M. S. (2012). AeroFlex: a toolbox for studying the flight dynamics of highly flexible airplanes. In *VII Congresso Nacional de Engenharia Mecânica (CONEM)*. São Luís, Brazil.

[20] Harder, R. L. and Desmarais, R. N. (1972). Interpolation using surface splines. *Journal of Aircraft*, 9(2), 189–191. doi:10.2514/3.44330.

[21] Chung, J. and Hulbert, G. M. (1993). A time integration algorithm for structural dynamics with improved numerical dissipation: the generalized-α method. *Journal of Applied Mechanics*, 60(2), 371–375. doi:10.1115/1.2900803.

[22] Jansen, K. E., Whiting, C. H., and Hulbert, G. M. (2000). A generalized-α method for integrating the filtered navier-stokes equations with a stabilized finite element method. *Computer Methods in Applied Mechanics and Engineering*, 190(3-4), 305–319. doi:10.1016/S0045-7825(00)00203-6.

ACKNOWLEDGMENT

This work has been supported in part by FINEP and EMBRAER under the research project Advanced Studies in Flight Physics, contract number 01.14.0185.00.

COPYRIGHT STATEMENT